The Localization by Topography of the Three-Dimensional Overturning Circulation of the Southern Ocean and Its Implications

Madeleine K. Youngs [1], **Glenn R. Flierl** [2]

[1]NYU, Courant Institute of Mathematical Sciences
[2]MIT, Department of Earth, Atmospheric, and Planetary Sciences

Key Points:

- This study develops a three-dimensional analysis of the Southern Ocean overturning circulation.
- The net overturning, shaped by winds, standing and transient eddies, occurs near topography.
- Local standing and transient eddy processes weakens the response of overturning to changes in wind.

Corresponding author: Madeleine K. Youngs, my2368@nyu.edu

Abstract

The Southern Ocean plays a major role in the global air-sea carbon fluxes, with some estimates suggesting it contributes to up to 40% of the oceanic anthropogenic carbon dioxide uptake, despite only comprising 20% of oceanic surface area. Thus the Southern Ocean overturning transport, the circulation that transports tracers between the surface and the interior, is particularly important to understand. Recent studies show that this vertical transport preferentially occurs downstream of bottom topography, but there is further work to understand how this relates to the theory of overturning circulation. This study uses an idealized Southern Ocean-like MITgcm channel and particle tracking in the thickness-weighted circulation to develop a new understanding of the three dimensional and localized nature of the overturning, splitting the flow into three main drivers of the transport. The first component is a wind-driven Ekman pumping into or out of a density layer; it is primarily but not entirely zonally-symmetric due to the meandering nature of the flow. The remaining two components are standing eddies and transient eddies both of which are localized near the topography. The existence of the ridge weakens the response of the overturning to changes in wind, especially in the lower cell. The localization of the vertical flow shows the necessity of careful modeling of these specific regions in the Southern Ocean to understand the transport, carbon export, and the connection with the oceans to the north.

Plain Language Summary

The Southern Ocean is a key location for the global carbon budget because it is where the deep ocean interfaces with the atmosphere and exchanges long-held carbon reserves. This study uses an idealized channel model to see how the surface ocean connects to the deep ocean and finds that almost all of this connection is right near the topographic features. The localization of the flow due to the undersea ridge reduces the sensitivity of the vertical and northward transport of the deepest water mass to changes in wind. This points to the importance of sampling and modeling these localized regions carefully in order to capture the global transport.

1 Introduction

The wind- and buoyancy-driven circulation in the Southern Ocean plays a primary role in setting the properties in the deep ocean, with important implications for global circulation and climate. For example, this region is responsible for about 30% to 40% of oceanic anthropogenic carbon uptake, an oversized contribution (Gruber et al., 2009; Frölicher et al., 2015). How that carbon budget has varied since the industrial revolution and how the budget will change with climate change are open questions (Le Quéré et al., 2017). Since there is a strong vertical gradient in dissolved inorganic carbon in the near-surface Southern Ocean (Gruber et al., 2009), the vertical transport of water is a major physical process affecting the air-sea carbon fluxes. The overturning circulation has been shown to be a leading component in controlling anthropogenic carbon (Ito et al., 2010). Thus an understanding of upwelling and downwelling into the deep ocean and how it responds to changes in wind patterns and strength is, therefore, necessary in analyzing the carbon budget.

Traditionally, we call the circulation responsible for the vertical and meridional transport of tracers the residual overturning circulation, because it is regarded as a small remainder of two main competing processes, wind-driven overturning that steepens isopycnals and eddy-driven overturning that acts to relax those isopycnals (Marshall & Speer, 2012). This understanding was developed for an idealized ocean that lacks bottom topography or other zonal asymmetries, although it permits them in a zonally-averaged sense. While Marshall and Radko (2003) discuss the fact that the residual flow need not be restricted to zonally symmetric flows, they revert to zonally-symmetric forcing and

no topography for building a conceptual picture of the overturning. This is then carried to global theory of circulation, like when Nikurashin and Vallis (2011) construct a global circulation scheme using a symmetric annulus for the Southern Ocean. Yet, many other aspects of this zonally-averaged theory have been shown to be overly simple due to the existence of topography (Youngs et al., 2017, 2019; Abernathey et al., 2011), leaving the question of how the topography modifies the overturning circulation and changes its response to variations in the winds or buoyancy forcing, not only in the zonally-averaged sense, but also in the way it might connect to the flows in other ocean basins.

Previous studies of how the overturning circulation varies with changes in wind have usually considered the steady state overturning and constant forcings (Hallberg & Gnanadesikan, 2006; Abernathey et al., 2011; Meredith et al., 2012). It is hypothesized that as the wind strengthens, the wind driven overturning strengthens and the isopycnal slopes steepen, leading to an increase in the eddy driven circulation, at least partially compensating for the change in the wind driven circulation (Marshall & Speer, 2012), a process called eddy compensation. However this is based on the zonally symmetric conception of the overturning (Abernathey et al., 2011), so we need to understand how the topography changes sensitivity of the overturning. There have been several studies about the sensitivity of the overturning to changes in wind with topography, but with limited results (Meredith et al., 2012; Zhai & Munday, 2014; Munday & Zhai, 2015; Bishop et al., 2016; Kong & Jansen, 2021). In addition, the sensitivity of the isopycnal slopes to changes in the wind has been examined in a 2-layer quasi-geostrophic channel (Youngs et al., 2019). There is still a gap with connecting the zonally-averaged theory of eddy compensation to how the sensitivity differs with a ridge and without.

The Southern Ocean State Estimate shows that in the multiyear mean regions of strong vertical velocity are isolated near topography (Figure 1), suggesting the importance of the topography for driving upwelling (Mazloff et al., 2010). This has been confirmed in similar models by showing particle upwelling localized to regions downstream of topography using a Lagrangian viewpoint of the circulation (Tamsitt et al., 2018; Viglione & Thompson, 2016). The localized upwelling has been suggested to be due to baroclinic eddies enhanced downstream of topography. Additionally downwelling is shown to be local as well with studies showing that Antarctic Intermediate Water and Antarctic Bottom Water are formed locally (Talley, 2013). However, we don't yet know how this local upwelling/downwelling picture connects to the zonally-averaged theory of the overturning. For that, we need to adapt the residual transport in the three-dimensional sense to discover where the transport is occurring and how strong it is.

In this study, we use an MITgcm channel model representing the Antarctic Circumpolar Current, with idealized geometry, topography, and forcings, to understand how the topography localizes the circulation. In this paper, we describe the numerical model and methods used to analyze the flow in section 2. In section 3 we present our results; in section 4 we discuss the dynamical processes occurring and the implications for climate models. In section 5 we conclude.

2 Method

2.1 Ocean Model

We investigate the full three-dimensional circulation around topography in the Southern Ocean using the simplest model that encapsulates the necessary complexity. We use an MITgcm channel that is 4000 km long by 2000 km wide and re-entrant in longitude (Figure 2). The model is run primarily at a 10 km resolution with select simulations at 5 km. The deformation radius in this configuration is about 15 km, but features tend to be larger than the deformation radius (Pedlosky, 1987), making this configuration adequately eddy-resolving. We have a total depth of 4000 m with 32 points in vertical, from

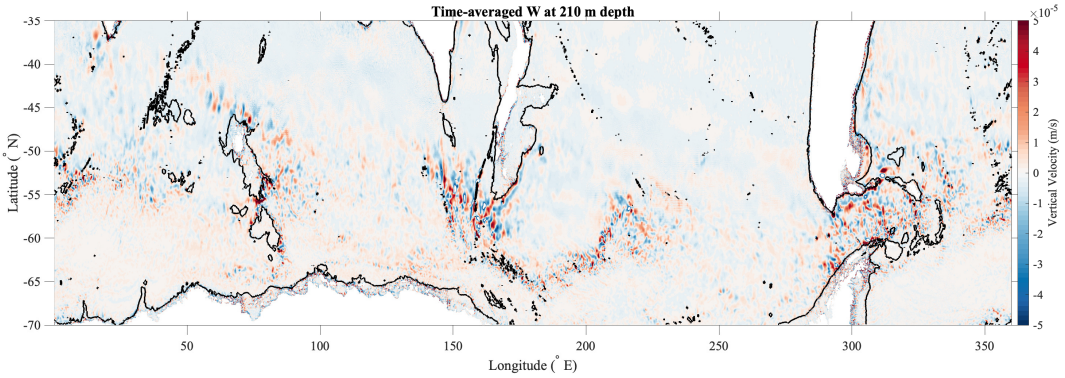

Figure 1. Vertical velocity at 210 m depth in the Southern Ocean State Estimate (SOSE) 1/6 degree simulation averaged from 2013 to 2018. The black contours show the 2000 m isobath showing the location of topography. Vertical velocity is not uniform across the Southern Ocean, but instead is enhanced near topographic features, countering the assumption of residual overturning theory that the circulation is uniform throughout the Southern Ocean.

10 m grid spacing at the surface to 280 meters in grid spacing at the bottom, as used in previous studies (Abernathey et al., 2011; Youngs et al., 2017). For topography we have a Gaussian ridge of half-width 200 km, 2000 m tall, located at 800 km downstream of the channel entrance (Figure 2) representing a characteristic undersea ridge over a 1/4 of the length of the Antarctic Circumpolar Current. We also run simulations with a flat bottom, as a representation of the zonally-averaged theory. We use a 600 second time step and a diffusivity varying from 0.01 $m^2\ s^{-1}$ to 1×10^{-5} $m^2\ s^{-1}$ with a tanh profile having a decay scale corresponding to a mixed layer depth of 40 m: $\kappa = 10^{-5}+(10^{-2}-10^{-5}) * (\tanh(z+40)-1)$. We also have a linear bottom drag with a drag coefficient of 1.1×10^{-3}m s^{-1} and free slip sides. We note here that we split up the domain into three regions: the upstream region ahead of the topography, the downwash region from 800 km to 2000 km, and the downstream region, 2000 km to the end of the domain (Figure 3). The downwash region is important because it is where the transient and standing eddies are active. We differentiate these regions following (Youngs et al., 2019), to give them a consistent definition.

2.2 Boundary Conditions

The surface is forced using a wind stress of the form

$$\tau(y) = \tau_0 \sin(\pi y/L_y) \tag{1}$$

where $L_y = 2000$ km. For the base case, $\tau_0 = 0.15$ N/m^2; it will be varied from 0.05 to 0.25 N/m^2 (Figure 2).

At the northern boundary, the temperature (which determines the buoyancy) relaxes to a fixed profile with a timescale of 1 week, as an exponential profile

$$T_n(z) = \Delta T(e^{z/z'} - e^{-H/z'})/(1 - e^{-H/z'}) \tag{2}$$

where T_n is the temperature at the northern boundary, H is the domain depth of 4000 m, and $-z'$ is a decay depth of 1000 m. The choice of profile is justified by Karsten and Marshall (2002) using observations. In addition this choice has been used in several other experiments (Abernathey et al., 2011; Stewart & Thompson, 2013) to permit high-resolution in the channel without the need of solving in the basin to the north. There is no heat flux through the bottom or the southern wall.

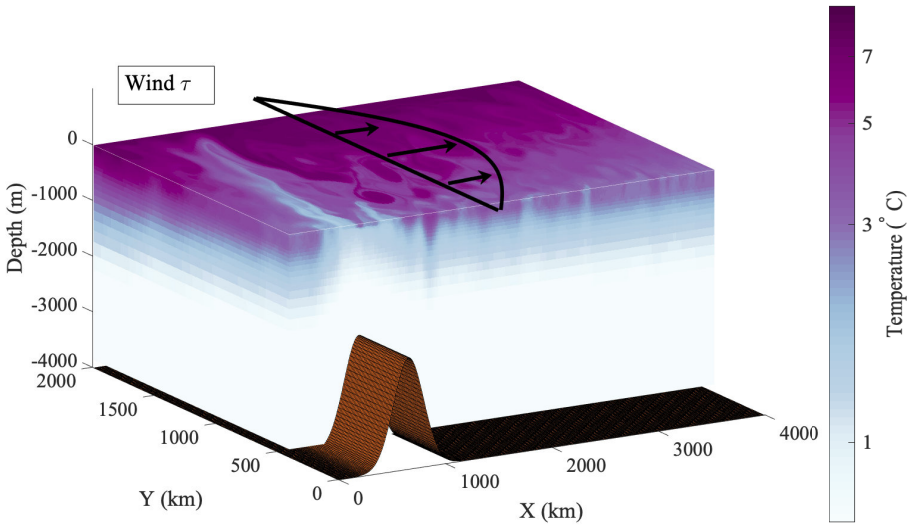

Figure 2. Geometry of the idealized MITgcm channel. There is a Gaussian ridge that is 2000 m tall located at 800 km, wind has a cosine profile with a maximum τ_0, the color here is a snapshot temperature with $\tau_0 = 0.15$ N m^{-2}. The ridge is a similar dimension and steepness compared to real topographic features in the Southern Ocean and the channel length of about 1/4 the size of the Southern Ocean approximates the spacing of major topographic features.

There are two main options for setting up surface heat flux conditions: a fixed flux condition where a prescribed amount of heat is put in or pulled out of the surface ocean, or a relaxation to a set temperature profile at the surface, where the amount of heat fluxed in or out of the surface is proportional to the difference of the surface temperatures from the selected profile (Abernathey et al., 2011). We use a surface relaxation condition for several reasons: it is a better representation of the air-sea exchange, and the overturning strengthens or weakens considerably more as the winds change than in the case of fixed-flux (Haney, 1971). In addition, the large meanders in sea surface temperature will indeed alter the air-sea flux of heat. Using a fixed surface relaxation temperature profile for both the flat bottom and ridge cases leads to wildly different overturnings; with the same relaxation profile for flat and ridge cases, one configuration or the other lacks one of the overturning cells. Instead we have adopted a method which allows both a relaxation boundary condition and comparable overturnings for the flat bottom and ridge simulations.

We set up the relaxation conditions following Abernathey et al.(2011). We first run simulations with a fixed flux surface boundary condition as shown in Figure 3(b) for both ridge and flat-bottomed cases. From these simulations, we use the time- and zonally-averaged surface temperature, $\langle T \rangle$ to choose a relaxation temperature profile $T_0(y)$ with a heat flux $Q = -\lambda(\langle T \rangle - T_0)$ where λ is the relaxation time scale of one month. In other words, we ran one flat and one ridge simulation to set the temperature relaxation profiles, then fixed the relaxation profiles in the wind perturbation experiments. This creates comparable overturning circulations as seen in Figure 5 while using different relaxation temperature profiles (Figure 3(c)).

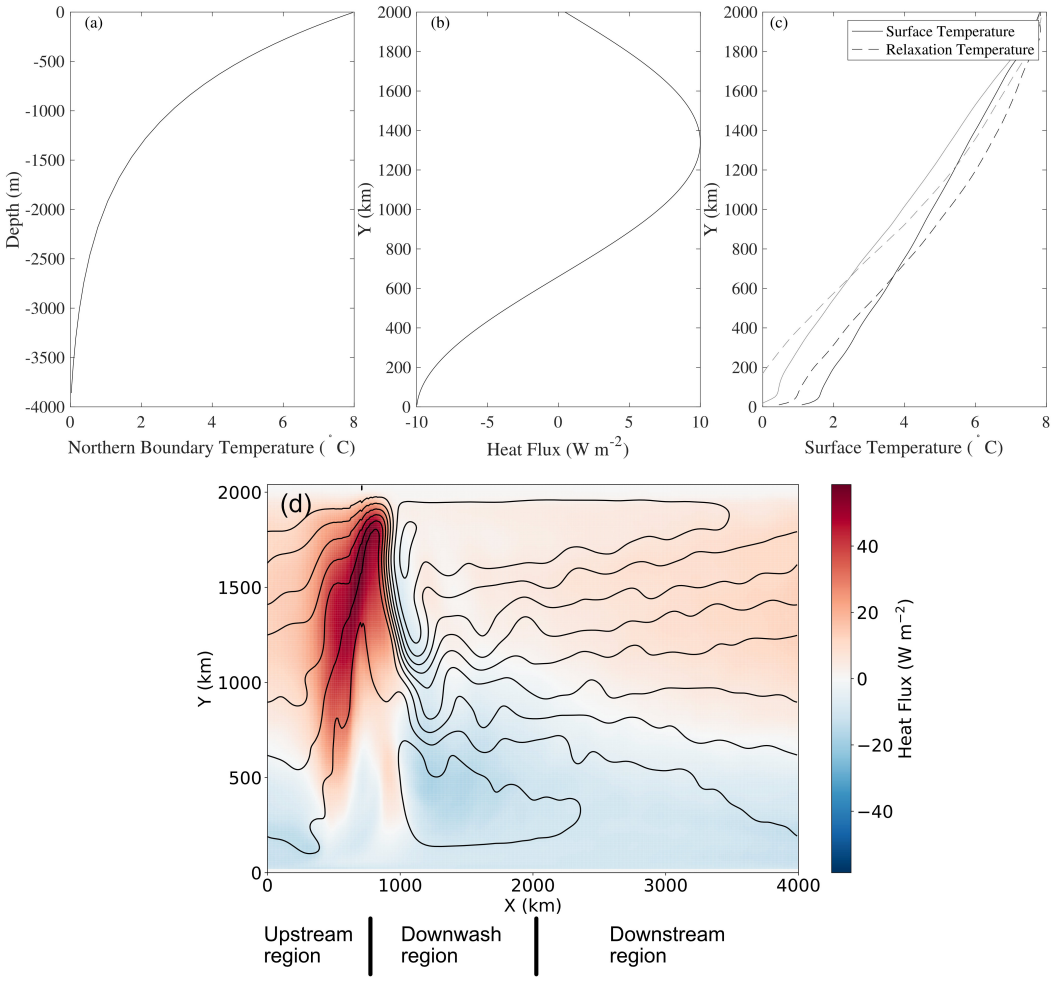

Figure 3. Figure showing the temperature boundary conditions. (a) Northern boundary relaxation temperature. The temperature is relaxed linearly from the maximum at the northern boundary, linearly scaling back to no forcing at 1930 km. (b) Heat flux profile used with the average surface temperature (c) to generate surface relaxation temperature with the temperatures in black representing the ridge simulation and grey representing the flat bottom simulation. (d) shows the full heat flux pattern for $\tau_0 = 0.15$ N m^{-2}. The black lines show the barotropic streamlines. From these forcings, we generate an upper and a lower overturning cell of reasonable strength relative to the channel length.

2.3 Thickness Weighted Circulation

We examine the spatial distribution of upwelling and downwelling, as well as determine the relative importance of the different components, by tracking particles in the thickness weighted mean velocity. This allows us to visualize the flow in x as well, moving beyond the zonally-averaged framework. Time-averaged thickness-weighted velocities are a generalization of the two-dimensional residual-mean theory to the local circulation. Visualizing just the vertical velocity in cross sections can be misleading because the local velocities were highest where there is a short residence time, partially canceling out the effect. Thus, we develop a method to visualize the local overturning circulation using the cumulative vertical displacement of Lagrangian particles advected in the thickness-weighted velocities.

We use the thickness-weighted horizontal and vertical velocities $\tilde{\mathbf{u}}$ as defined by Young (2012). This choice was made because the mean velocities are not parallel to the mean buoyancy surfaces (the Reynolds' heat fluxes imply that $\overline{u} \cdot \nabla \overline{b} \neq 0$), and, therefore, using them to advect particles would not represent the transport of tracers, because they do not include the flux by the time-varying flow. In contrast, the thickness-weighted velocities ensure that the particles stay on the mean buoyancy surfaces and are advected by both the Eulerian and time-varying flow. The thickness-weighted average is

$$\hat{\gamma} = \frac{\overline{\gamma h}}{\overline{h}} \tag{3}$$

where h is the thickness of a layer defined by $d^3\mathbf{x} = dx\,dy\,dz = h\,d\tilde{x}\,d\tilde{y}\,d\tilde{b}$, where the $\tilde{\cdot}$ indicates buoyancy coordinates and γ is an arbitrary variable. The overbar represents a time-average. Properties are interpolated to buoyancy (equivalent to temperature) surfaces, multiplied by the instantaneous thicknesses, h, and then time-averaged. The height of the buoyancy surface is given by

$$z = \zeta(\tilde{x}, \tilde{y}, \tilde{b}, \tilde{t}) \tag{4}$$

where ζ defines the buoyancy surface. The three-dimensional thickness-weighted velocities are given by

$$\tilde{\mathbf{u}} = \left(\frac{\overline{hu}}{\overline{h}}, \frac{\overline{hv}}{\overline{h}}, \frac{\overline{hu}}{\overline{h}}\overline{\zeta}_{\hat{x}} + \frac{\overline{hv}}{\overline{h}}\overline{\zeta}_{\hat{y}} \right) \tag{5}$$

The $\hat{x}$, $\hat{y}$ derivatives are taken in buoyancy space. The advective derivative for θ looks the same as usual, but with the $\tilde{\mathbf{u}}$ velocities.

The contribution to the vertical displacement from the time-varying flow is simply the difference between advection by the Eulerian-mean $\overline{\mathbf{u}(\mathbf{x})}$ and by the thickness-weighted mean $\tilde{\mathbf{u}}$. We use the "layers" package to calculate $\overline{uh}, \overline{vh}, \overline{h}, \overline{u}, \overline{v}$ on temperature layers or in $(\tilde{x}, \tilde{y}, \tilde{b}, \tilde{t})$-coordinates. The time-averaged temperatures are used to calculate $\overline{\zeta}_{\tilde{x}}$ and $\overline{\zeta}_{\tilde{y}}$. The thickness-weighted averages $\hat{u}$, $\hat{v}$, $\overline{\zeta}_{\tilde{x}}$, and $\overline{\zeta}_{\tilde{y}}$ are transformed back into (x, y, z, t)-coordinates. From this we calculate $\tilde{\mathbf{u}}$ and release and track particles in this velocity field.

The computation is done using standard Lagrangian equations for movement in a specified flow field. To understand why using this is appropriate with the thickness-weighted mean velocities, we note that the solution to the passive tracer equation

$$\frac{\partial}{\partial t}\theta + \tilde{\mathbf{u}} \cdot \nabla\theta = 0 \tag{6}$$

with a delta function initial condition is

$$\theta = \delta(\mathbf{x} - \mathbf{X}(t)) \tag{7}$$

where $\mathbf{X}(t)$ gives the position of the particle moving according to $\tilde{\mathbf{u}}$. Therefore, the particles show where and how fast water is upwelling or downwelling within a density layer.

Computationally, particles generally stay on buoyancy surfaces; those that do not because of diabatic processes in the surface layer or interpolation errors are discarded. Thus, the vertical velocities calculated here are purely adiabatic and along isopycnals.

2.4 Particle Tracking

In order to visualize the three-dimensional overturning we track particles in the thickness-weighted velocities. We release particles at $x = 100$ km and every y and z location on the native grid, near the entrance to the channel and advect the particles using an RK-2 advection scheme in the time-mean thickness-weighted velocities. They are advected from the entrance of the channel until they either exit the domain to the east or run into the diabatic region in the north. We discard particles that enter the mixed layer, and those that enter the northern temperature relaxation region. The particles are catalogued based on the initial temperature and eliminate particles if they enter the forcing regions at the north or surface. We calculate the total displacement experienced by a particle advected in the thickness-weighted flow and then show the vertical displacement following these particles in figure 4. The particles go up and down over the topography and then generally see enhanced upwelling downstream of the topography, in the downwash region, and then a leveling out far downstream. The upwelling and downwelling seen in these chosen temperature layers is reflective of the overturning circulation calculated for figure 5.

Next, we average over the latitudes (Y) in each temperature layer to understand the cumulative upwelling versus position down the channel, allowing a visualization of the upwelling surface (Figure 7). We examine the cumulative displacements because the local upwelling is difficult to visualize due to horizontal velocities (and thus residence times) varying significantly across the domain. The vertical displacement is divided by the total time it takes to transit the domain, in part because the total displacement in one transit of the channel is much larger for the colder temperature layers because the transit time is much slower. The transit time is about 2 years for the warmer layers, but closer to 9 years for the colder layers. Dividing by the mean total time of each temperature layer allows a clearer comparison between the different temperature layers. We call this component of the vertical displacement in the thickness-weighted velocity is the total displacement because it includes all of the components defined below.

To calculate the mean displacement, we tabulate the vertical displacement from just the Eulerian mean velocity in depth space. The particles are still advected in x, y, z using the full thickness-weighted flow, but the vertical displacement is calculated with the local Eulerian mean w by multiplying by the time step and adding it to calculate the mean displacement. In other words, this is the cumulative integral of the Eulerian mean vertical velocity experienced by the particle. In addition we calculate the transient eddy component defined as the difference between the Eulerian mean and the full thickness-weighted component. Then we can split up the Eulerian mean displacement into two different components, the Ekman displacement and the standing eddy displacement. The Ekman displacement is the displacement calculated using the Ekman velocities ($w = \frac{1}{\rho_0 f^2}(\tau_y f - \tau\beta)$), assuming they are the same at every depth. This is a fair assumption because the scale depth, or the depth that the surface circulation is felt, is much deeper than the ocean bottom. The standing eddy term is the difference between the Eulerian mean and the Ekman displacement and it represents the displacement due to deviations from the zonal average flow (in the time average). This split of components is validated in the ridge-free simulations, which represent the zonally-averaged circulation, because the Eulerian mean displacement is dominated by the Ekman displacement (Figure 8).

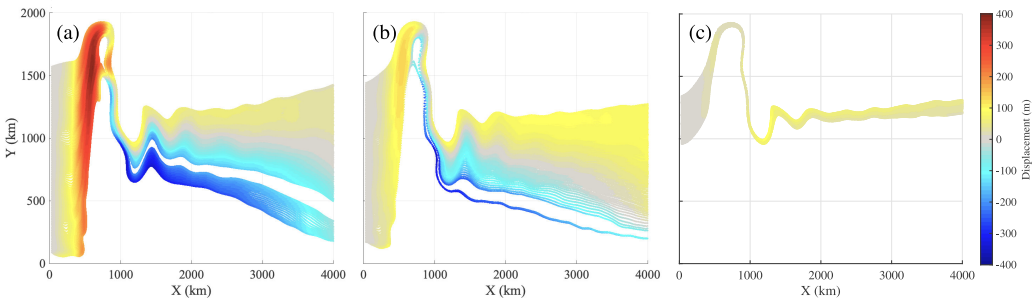

Figure 4. A figure showing the total displacement on three different temperature surfaces, representing the three different overturning branches that we can resolve. We release particles at the western boundary of the domain and follow them to calculate their displacement relative to their initial z positions. (a) shows particles released at 1 C, which represents lower cell downwelling. (b) shows particles release at 2 C which represents lower cell upwelling. (c) shows particles released at 4 C which represents upper cell upwelling. The upwelling and downwelling seen here is reflective of that seen in Figure 5. Particles move north and south due to the ridge and experience different vertical transport depending on their location.

3 Results

3.1 Overturning Calculation

The first way we analyze the flow is by calculating the traditional residual overturning and how it varies with the wind stress. We can calculate the residual overturning as follows:

$$\psi = \int_0^{T'} \int_0^{x_{max}} \overline{vh} dx dT \tag{8}$$

where h is the temperature (buoyancy) layer thickness, v is the meridional velocity in the layer. We show the residual overturning circulation for both the flat bottom and ridge cases (Figure 5). One major difference between the flat and ridge cases is that the heat fluxes are not zonally symmetric and are visibly enhanced near topography due to colder water being brought northward (Figure 3(d)). A meander here is a north/south deviation of flow in the time-mean. The circulations within the meander envelope shown by the dashed lines in Figure 5(c) represent surface processes. This is shown by the blue, negative cell entirely within the envelope of surface temperatures seen at the same latitude but at different longitudes or times. When this feature is then projected into depth-space using the zonally-averaged isopycnals, the surface meander feature ends up partially below the surface ocean, appearing to show a non-existent diabatic process at depth. In reality, because of the lack of diabatic mixing, cross-isotherm transport has been shown to be minimal in configurations like this (Marshall & Speer, 2012; Marshall & Radko, 2003). Due to this, we would regard the 'true' overturning as that seen in the northern third of the domain. The vertical isopycnal seen at the southern wall in Figure 5(d) is an artifact of the meander as well, because that colder temperature reaches the surface only over the topography.

Isopycnal slopes are much steeper for the flat-bottomed simulations, leading the lower cell to be much deeper in the flat-bottomed simulations than with the ridge simulations (Abernathey & Cessi, 2014). This has implications for which water masses reach the surface and where they are exchanged with the rest of the ocean. In addition, the

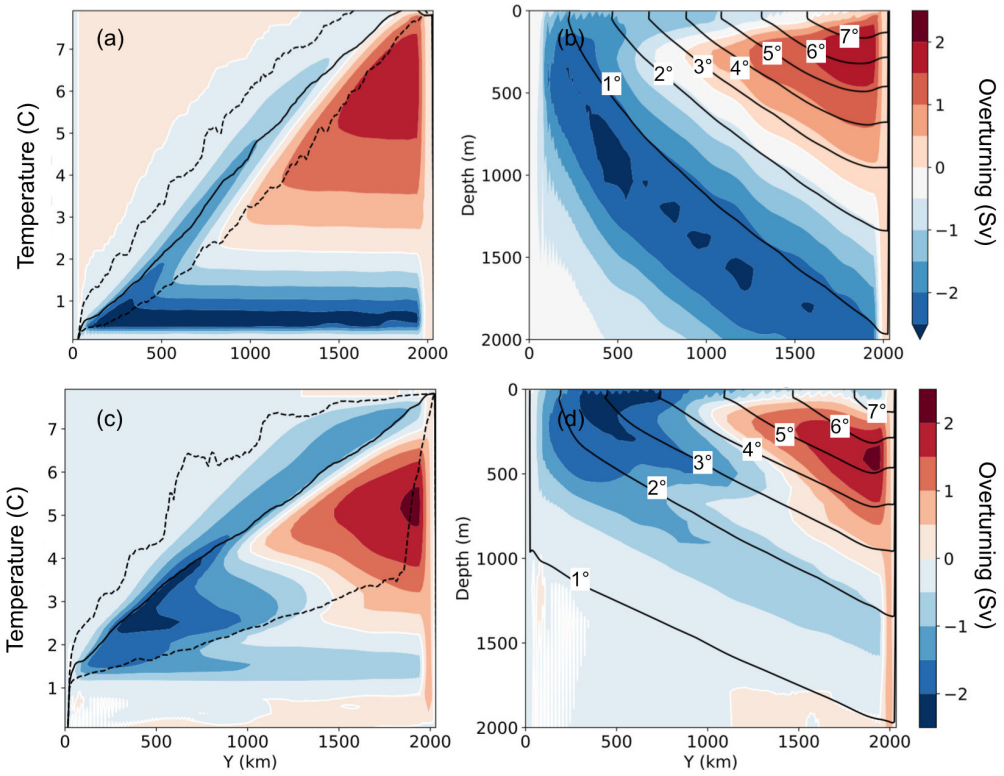

Figure 5. Residual overturning in temperature space (a,c). The same overturning projected into depth coordinates (b,d). The overturning is shown for flat-bottomed simulations (a,b) and ridged simulation (c,d). The solid black (a,c) line shows the mean surface temperature versus Y, and the dashed lines show the 1 and 99 percentile of temperature values, representing the temperatures exposed to the surface. The solid black lines (b,d) show the mean isopycnals. These show similar overall magnitude of the residual overturning for both flat-bottomed and ridge simulations, but with an additional feature in the lower cell in the ridge simulations due to the meandering flow over topography.

baroclinicity of the flow is on average higher in the zonally-symmetric flow, but locally significantly higher for the ridge configuration.

We split up the overturning into different cells and branches to isolate the dynamical processes for the upwelling branch of the lower cell and the upper cell and the downwelling branch of the lower cell. We can isolate these branches based on the temperatures of the overturning in temperature space in the ocean interior, which corresponds to the northern-most section of the domain in Figure 5(c) where the overturning contours are flat. The lower cell downwelling is the coldest temperatures seen to the maximum in the lower cell overturning as seen close to the northern boundary. The lower cell upwelling is the temperature range between the maximum of the lower cell and the sign change of the overturning, again along the northern boundary. The upper cell upwelling is defined by the temperature range from the sign change to the maximum of the overturning seen at the northern boundary.

3.2 Sensitivity to Wind

The addition of a ridge modifies the sensitivity of the overturning to changes in wind stress. Figure 6 shows how the overturning strength changes as the wind stress increases or decreases for both flat-bottomed simulations and ridged simulations. We see that the sensitivity to the wind stress is very similar for the upper cell for both cases, but the lower cell responds differently, with the flat bottom lower cell magnitude weakening significantly, and with a ridge, the overturning doesn't significantly change. As a validation of the model resolution, we also ran the simulations at a 5 km resolution and saw the same physical behavior: with a ridge, the lower cell overturning hardly changes at all as the wind changes, unlike with a flat bottom. Thus, the topography significantly alters the sensitivity of the overturning. We will discuss more the potential dynamical process at play in Section 4.

How the isopycnal slopes change with the wind is related to the changes in overturning strength due to shifting surface outcrop positions, changing the strength of the heat flux. For the slopes of the upper cell, the flat bottom slopes vary quite a bit as the wind stress increases, but when there is a ridge, the upper cell slope approaches a constant value (Figure 6). This agrees with results seen in Youngs et al. (2019). As the winds increase beyond a certain value, all of the wind changes are absorbed by the standing meander. For the lower cell, the flat bottom isopycnal slopes increase with the wind. For the ridge, the isopycnal slopes decrease as the winds increase. The reasons for this are laid out in Youngs et al. (2019), but it relates to how the meander strengthens as the wind stress increases. These isopycnal slope changes thus dictate how the overturning changes with the wind.

3.3 Overturning Displacements

3.3.1 Eulerian Mean Versus Transient Eddies

Now we investigate the three-dimensional circulation using the method described in section 2.3. The cumulative vertical displacement on temperature surfaces of particles transiting the domain west to east is shown in Figure 7. In Figure 7(a,b,c) we show the cumulative displacement in the ridge simulations and in panels (d,e,f) we show the comparison to the flat-bottomed simulations as a representation of the zonally-averaged circulation. The total upwelling is shown in panels (a) and (d), the Eulerian mean (b) and (e), and the transient eddies (c) and (f). First we examine the total upwelling with a flat bottom (Figure 7 (d)) which shows us the same pattern but with a purely linear increase, indicating the zonally symmetric nature of the flat-bottomed simulations. Also for the flat bottom, the Eulerian mean (e) and the transient eddies (f) have opposing signs so that the total is a small residual. As expected we see the mean component balanced by a transient eddy component in the case without a ridge (Abernathey et al., 2011) but see zonal asymmetric configuration in the case with a ridge. These differences are explainable due to the existence of the topography in the ridge case.

For the ridge case, most of the structure comes from the area right around the ridge (Figure 7 (b)). The total upwelling has a very localized pattern with peaks located near the topography and in the downwash region at 1200 km (Figure 7 (a)). By the end of the domain, we see the upwelling and downwelling we expect, with a net upper cell upwelling at the temperatures expected by looking at the meridional overturning in the presence of a ridge (Figure 5 (c)), and a similar correspondence for the lower cell upwelling and downwelling. Thus the trajectory-based calculations recover the total overturning calculated in the usual way. We can see the effects of the wind-driven zonally-symmetric component in the downstream regions by the smooth uniform upwelling and downwelling, which is what we expect for a uniform-wind driven upwelling. The transient eddies (Figure 7(c)), on the other hand are localized in the downwash region, where they lead to upwelling or downwelling in one location and then nothing changes for the rest of the domain. Thus, the lower cell downwelling is driven by the transient eddies and the Eu-

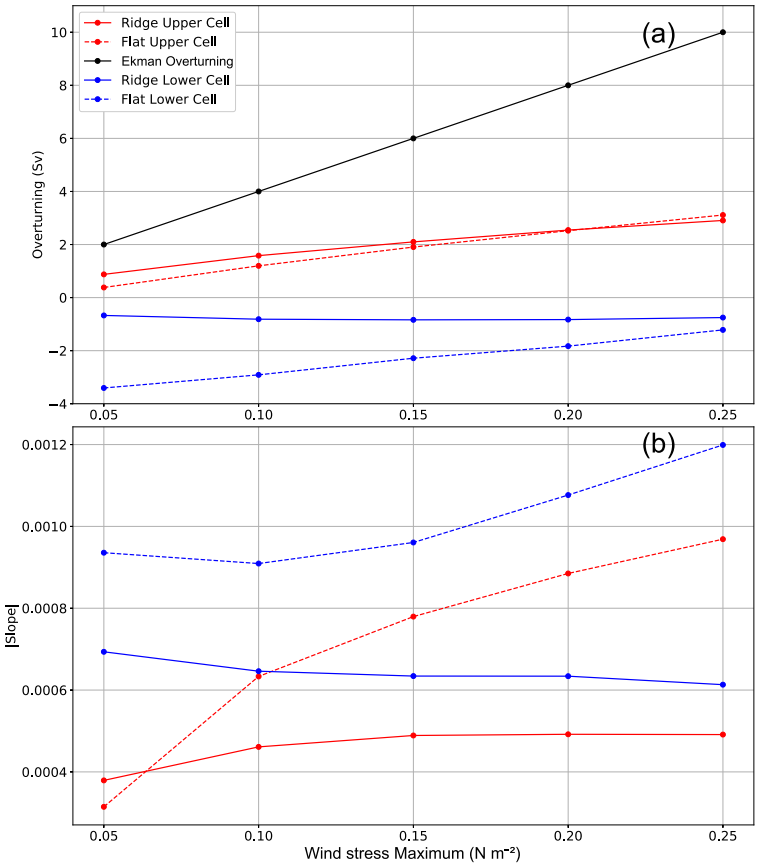

Figure 6. The overturning versus the wind stress maximum for both the flat-bottomed and the ridged simulations (a) and the isopycnal slopes calculated locally and then averaged for each cell (b) averaged over 40 years. The wind-driven component is the Ekman component calculated via scaling $\frac{\tau}{\rho_0 f}$. We show here that the sensitivity is much weaker for the lower cell when we have topography indicating that the zonal asymmetry (the ridge) is important for the sensitivity. The change in overturning is in part understood by the changes in isopycnal slopes, whose response is studied in detail in Youngs et al. (2019).

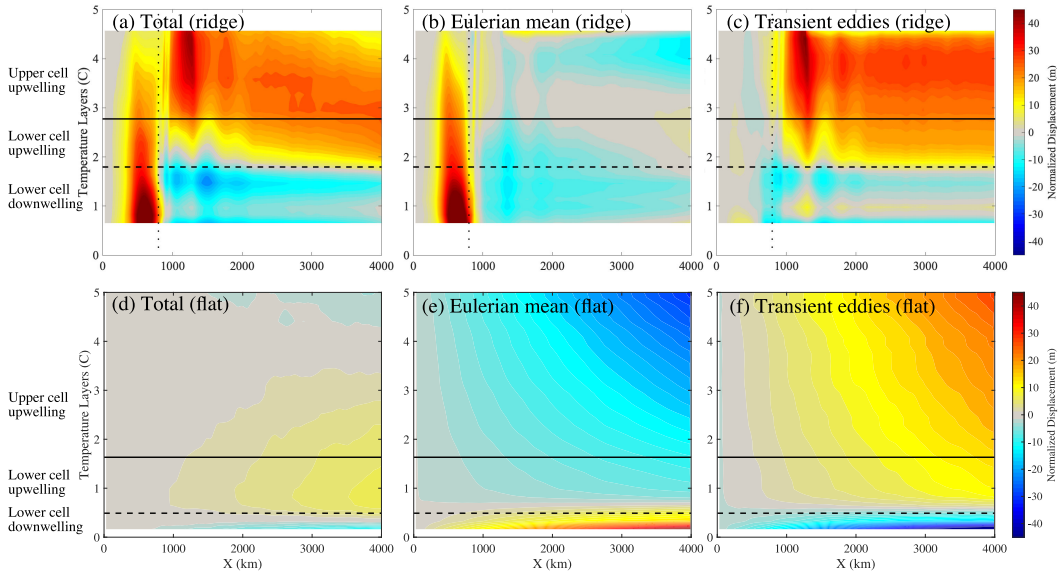

Figure 7. An analysis of the displacement of particles for a ridge case (a,b,c) and a flat bottom (d,e,f). We then split up the flow from the total overturning (a,d) into the Eulerian mean (b,e) and transient eddies (c,f), where the vertical advection of each component is catalogued separately. The displacement is normalized by the total amount of time to transit throughout the domain and multiplied by the mean for all particles. The solid line indicates the separation between the upper and lower cells and the dashed line separates the upwelling branch from the downwelling branch as diagnosed from Figure 5 (a,c). The dotted line shows the location of the ridge crest This shows us that the transient eddies are localized strongly in the downwash region (X = 1000 km), although the mean component is leading order for the lower cell upwelling. For the ridge case, the total is not a small residual between the winds and the other components.

lerian mean, whereas the lower cell and upper cell upwelling is primarily driven by different processes, which has implications for how the overturning changes with the wind stress.

3.3.2 Understanding the Eulerian Mean Overturning

From Figure 7, the pattern of the Eulerian mean vertical transport seems to have multiple components, one localized near the topography and one gradually, linearly, increasing or decreasing throughout the domain. To further investigate this, we split the Eulerian velocity into Ekman velocity and the remainder, arising from the standing eddies, and compute the displacement. In Figure 8(a,b,c) we show the cumulative displacement in the ridge simulations and in panels (d,e,f) we show the comparison to the flat-bottomed simulations as a representation of the zonally-averaged circulation. The Eulerian displacement is shown in panels (a) and (d), the Ekman displacement (b) and (e), and the remainder, the standing eddy component (c) and (f). This split is then validated in the flat bottomed case where almost all the Eulerian displacements are Ekman displacements (Figure 8).

For the ridge case, much of the structure is driven by the standing eddy component which only acts ahead of and just downstream of the ridge. For the Ekman component, we note that the wind-driven upwelling (mass flux in isopycnal layers) from the Ekman velocity is not entirely zonally-symmetric in the ridge case because the isopyc-

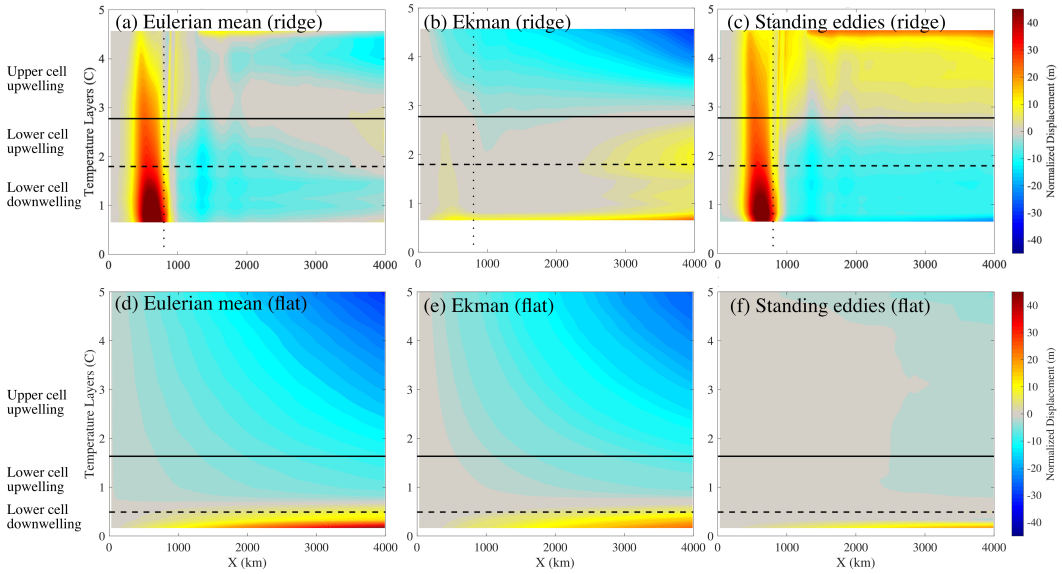

Figure 8. An analysis of the Eulerian-mean displacement of particles for a ridge case (a,b,c) and a flat bottom (d,e,f). We then split up the flow from the mean displacement (a,d) into the Ekman (b,e) and standing eddy (c,f), where the vertical advection of each component is catalogued separately. The displacement is normalized by the total amount of time to transit throughout the domain. The Ekman component is dominant in the upper cell upwelling whereas the standing eddy component is dominant in the lower cell.

nal slopes vary so much through out the domain, leading to a north and south-ward excursion of the temperature surfaces, changing the wind forcing in x along an isopycnal. Thus, the Ekman velocities are the same for the flat and the ridge case, but the upwelling generated by the same velocities are different because of the different thermal structures.

4 Discussion

In this paper we have examined the role of topography in modifying the fundamental overturning circulation, including the three-dimensional nature of the overturning as diagnosed using the new technique we present.

4.1 Role of the Standing Eddy

The standing eddy component has been shown to be an important part of the overturning circulation. In our case the standing eddy circulation is the difference between the Eulerian mean and the Ekman component, whereas the standing eddy is defined as the deviation from the zonal average in other studies (Bishop et al., 2016; Dufour et al., 2012). The standing eddy component shows an enhanced displacement upstream of the topography (Figure 8 c) and then a significant local downwelling in the lower cell, and local upwelling in the upper cell. Several studies in realistic geometries highlight the role of this component and its leading order nature, and we again find this to be the leading order of the overturning.

We have made an argument for why the isopycnal slopes change with changes in wind and how that alters the surface buoyancy fluxes. There is still a remaining gap here about which dynamical components of the overturning respond to changes in wind. In

eddy permitting models, several studies find that the standing eddies absorb the changes in the wind (Dufour et al., 2012; Bishop et al., 2016). In addition, standing eddies have been shown to sharpen in response to changes in wind stress (Thompson & Naveira Garabato, 2014). A similar analysis could be done with the methods shown here, but are outside the scope of this paper.

The standing eddy component is especially important in the lower cell. Since the standing eddy effectively absorbs changes in the wind (Bishop et al., 2016), it is consistent that there would be little change in the overturning with changes in wind. On the other hand, the processes driving the upper cell are more similar to the flat bottom channel with a wind stress balanced by transient eddies, so the upper cell's response to the wind is about the same in the presence of the ridge. Thus it seems that the differing driving processes in the upper and lower cell have different sensitivities to the wind, meaning that all three components of the overturning's sensitivity need to be modeled correctly in order to produce an appropriate overall sensitivity.

4.2 Metrics for Evaluating Models

4.2.1 Localized Enhanced Diffusivities

The localization of eddies just downstream of the ridge is very important for how the system responds to winds. The enhanced local eddy activity is responsible for the way the isopycnal slopes are affected by the wind strength. In addition, the enhanced localized eddy activity is also evident with eddy-driven upwelling in the vicinity of the topography (Figure 7). The enhanced local eddies are also evident in observations and more realistic models (Hogg et al., 2015; Bishop et al., 2016). This increased eddy activity leads to elevated eddy diffusivities near the topography (Abernathey & Cessi, 2014; Sallee et al., 2011).

Since the local eddy activity and thus localized enhanced eddy diffusivities are fundamentally important in setting how the system responds to changes in forcing, it is consistent that the local diffusivities would be an important factor in sensitivity. In a comprehensive review of modeling studies examining how the overturning changes with wind, Gent (2016) finds that model configurations where the Gent-McWilliams parameters were allowed to vary in latitude and longitude, based on the local stratification, are less sensitive to changes in wind. This is because the localization of the eddy activity becomes part of the parameterized Gent-McWilliams diffusivity. Allowing a spatially variable diffusivity suggests a way forward to make sure climate models appropriately respond to changes in wind stress (Kong & Jansen, 2021).

4.2.2 Three-dimensional Signatures in Zonally Averaged Diagnostics

Now that we have demonstrated the three-dimensional structure to the overturning in section 3, we ask if it is possible to see this signature in the standard zonally-averaged diagnostics. We show in Figure 9 the overturning calculation split into the Eulerian mean and the eddy components for the flat bottomed and ridge cases. We note that for the ridge case, the total in this zonally averaged framework is a small residual of the Eulerian-mean and eddy components, in contrast to the particle tracking diagnostics where the total, Eulerian-mean, and eddy components are all the same magnitude (Figure 7). The total overturning is set overall by the surface and northern boundary conditions. The Eulerian mean is dominated by the wind stress and is larger than the thermal boundaries can support. So the eddies must offset it the wind-driven transport, and do so differently between cases. In the flat-bottomed case, the eddies act uniformly along the channel, but with the ridge case the eddies are all focused near the ridge. The main difference between the ridge and flat cases are the vertically-banded features in the Eulerian mean and the eddy overturning for the ridge case due to the zonal asymmetry.

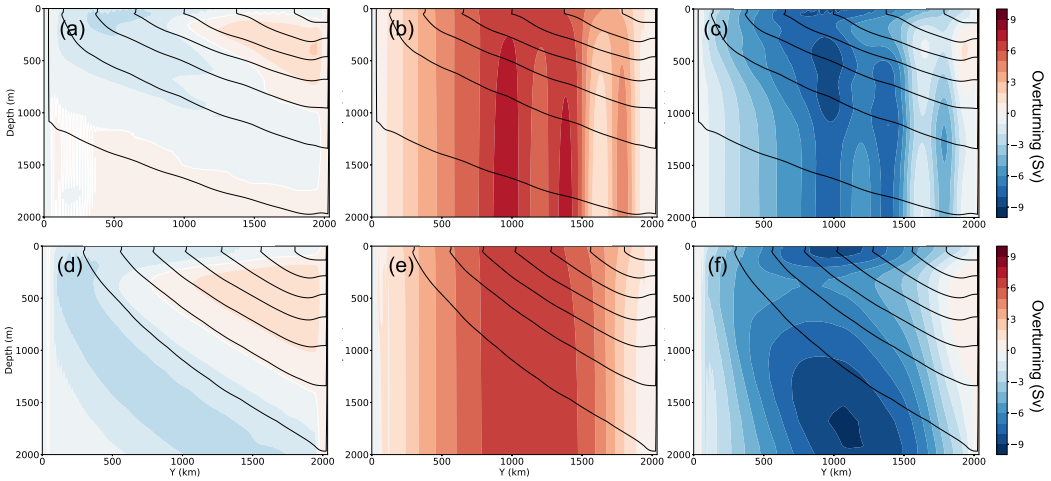

Figure 9. The meridional overturning (a,d) split up into Eulerian mean (b,e) and eddy (c,f) components for the ridge (a,b,c) and flat bottom (d,e,f) cases. This shows us that the zonally averaged diagnostics don't show many signatures of the localization, and over-estimate the contribution of wind-driven overturning.

This leaves the question, why is the Eulerian-mean component so much smaller, relatively, for the particle tracking diagnostics. We suggest that this is due to the particles traveling north and south throughout the domain experiencing the Ekman velocities in varying degrees depending on their position in y. In addition we average over y in a temperature layer, leading to partial cancellation in the north and south. This effect is larger for the ridge case because of the flatter isopycnals. Thus there is relatively little signal of the zonal-asymmetry in the zonally averaged diagnostics. This highlights the need for caution when analyzing the Eulerian mean overturning because it over-represents the role of the wind-driven overturning.

Calculating the mean overturning on isopycnals instead, may produce more fruitful results and the split into standing and transient eddies may bring more insights (e.g. Bishop et al., 2016). Alternatively, one other technique is calculating the zonal average along streamlines(Viebahn & Eden, 2012). This acts to transfer the contribution of the standing eddy component to the transient eddy component. However, there are many different ways to choose the streamlines, which are not necessarily a well defined. Even if they were well defined, the computations required are not straightforward either. For these reasons, we average along constant latitudes, which also has the added effect of quantifying the role of standing eddies, which are a robust important dynamical feature, rather than averaging over them so they disappear.

5 Conclusions

Throughout this study, we have connected localized particle upwelling to the thickness-weighted averaged circulation theory using an idealized Southern Ocean-like channel. We have shown that the zonally-averaged residual overturning is an insufficient picture because of the localized nature of the overturning (Figure 10) as highlighted using the technique developed to interpret the three-dimensional thickness-weighted circulation. The zonally-averaged overturning looks the same between the ridge (zonally-asymmetric) and flat-bottomed (zonally-symmetric) case because of the constraining nature of the forcing. However, the topography dramatically reduces the sensitivity of the lower cell over-

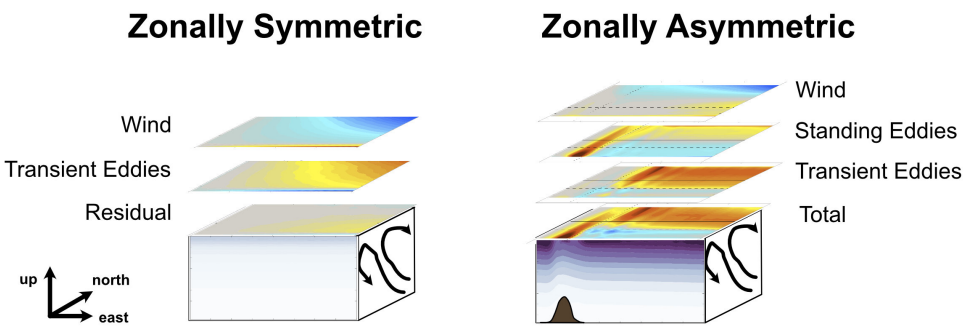

Figure 10. This figure schematically shows how our understanding of the overturning circulation changes with the addition of a zonal asymmetry due to topography. The colors on the surface represent the vertical displacement as a particle travels west to east across the domain and the arrows on the side represent the zonal average of the circulation. The zonally-asymmetric understanding highlights the role of the time-mean circulation via the standing eddy as a leading order feature of the overturning circulation, as well as the localized nature.

turning to changes in wind. This is related to how the isopycnal slopes evolve with the wind (Youngs et al., 2019). Including the topography is essential for predicting the sensitivity, in agreement with studies that show that the standing meander is primarily responding to changes in wind (Dufour et al., 2012; Bishop et al., 2016).

Extending the zonally-symmetric picture to three-dimensions with thickness-weighted circulation improves our understanding of the meridional overturning by showing definitively that upwelling near topography is in fact driven by predominantly transient eddies in the downwash region. We also provide a physical explanation for why the overturning changes the way it does with wind when there is a ridge, providing clarity to the discussion of eddy compensation, since it is likely that standing eddies absorb much of the change of the wind. In addition, a word of caution is given about using zonally-averaged diagnostics, because they over-represent the role of wind-driven transport in particular density layers in the channel with topography. A better theoretical understanding of have eddies develop in baroclinic flow around/ across the ridge would be very valuable. We believe that experiments like ours can provide insight into the spatial/temporal development of the transient eddies and their impact on the time-mean flows.

One limitation to generalizing these results is the idealized geometry, which provides a clear picture of the overturning but leaves out many other factors such as the Drake Passage restriction, other topography, ice, feedback from coupling to the north, etc. While we expect the importance of the standing meanders in the overturning and the response to wind changes and the fact that eddy compensation does not occur locally will still apply in a more realistic geometry, more investigations are necessary to tie the theory to the circulation. Another particular caveat involves the Southern Ocean lower cell. In the ocean, Antarctic Bottom Water occurs primarily at two very localized places, the Weddell and Ross seas (Talley, 2013; Rintoul, 2018). We do not replicate that localization or the specific overflow processes that generate the water mass. In addition the lack of atmospheric coupling is another limitation because of the importance of the local air-sea heat fluxes represented by the surface relaxation condition. This amount of specificity and detail was outside the scope of this project, but we suggest doing a similar analysis in more complex models that represent these processes.

Our study emphasizes that localization and a full three-dimensional analysis of transport is fundamental for the global overturning, but we remark that this localization is also fundamental for where carbon and other tracers upwell into the mixed layer. As highlighted in Youngs (2020), the flow near the ridge leads to very specific patterns of carbon outgassing. This suggests the necessity of highly-localized in situ measurements above topography to appropriately sample the carbon budget and vertical transport in the Southern Ocean. The methods outlined here have provided a better dynamical understanding of the relevant overturning processes in the three-dimensional Southern Ocean and can be used to analyze the three-dimensional circulation in more complex models.

Acknowledgments

We acknowledge helpful discussions with Mara Freilich, Andrew Stewart, David Marshall, Nicole Lovenduski, and Michael Spall. MKY acknowledges funding from the National Defense Science and Engineering Graduate Fellowship and the NOAA Climate and Global Change Postdoctoral Fellowship and NSF OCE-1536515. GRF acknowledges funding from NSF OCE-1459702. The code used to run the model is available at https://doi.org/10.5281/zenodo.4730
The SOSE output is available at sose.ucsd.edu. Computational resources for the SOSE were provided by NSF XSEDE resource grant OCE130007 and SOCCOM NSF award PLR-1425989.

References

Abernathey, R. P., & Cessi, P. (2014). Topographic Enhancement of Eddy Efficiency in Baroclinic Equilibration. *Journal of Physical Oceanography*, *44*(8), 2107–2126. doi: 10.1175/JPO-D-14-0014.1

Abernathey, R. P., Marshall, J., & Ferreira, D. (2011, dec). The Dependence of Southern Ocean Meridional Overturning on Wind Stress. *Journal of Physical Oceanography*, *41*(12), 2261–2278. Retrieved from `http://journals.ametsoc.org/doi/10.1175/JPO-D-11-023.1` doi: 10.1175/JPO-D-11-023.1

Bishop, S. P., Gent, P. R., Bryan, F. O., Thompson, A. F., Long, M. C., & Abernathey, R. P. (2016). Southern Ocean Overturning Compensation in an Eddy-Resolving Climate Simulation. *Journal of Physical Oceanography*, *46*(5), 1575–1592. doi: 10.1175/JPO-D-15-0177.1

Dufour, C. O., Le Sommer, J., Zika, J. D., Gehlen, M., Orr, J. C., Mathiot, P., & Barnier, B. (2012). Standing and transient eddies in the response of the southern ocean meridional overturning to the southern annular mode. *Journal of Climate*, *25*(20), 6958–6974.

Frölicher, T. L., Sarmiento, J. L., Paynter, D. J., Dunne, J. P., Krasting, J. P., & Winton, M. (2015, jan). Dominance of the Southern Ocean in anthropogenic carbon and heat uptake in CMIP5 models. *Journal of Climate*, *28*(2), 862–886. Retrieved from `http://journals.ametsoc.org/doi/10.1175/JCLI-D-14-00117.1` doi: 10.1175/JCLI-D-14-00117.1

Gent, P. R. (2016). Effects of southern hemisphere wind changes on the meridional overturning circulation in ocean models.

Gruber, N., Gloor, M., Mikaloff Fletcher, S. E., Doney, S. C., Dutkiewicz, S., Follows, M. J., ... Takahashi, T. (2009, mar). Oceanic sources, sinks, and transport of atmospheric CO2. *Global Biogeochemical Cycles*, *23*(1), n/a–n/a. Retrieved from `http://doi.wiley.com/10.1029/2008GB003349` doi: 10.1029/2008GB003349

Hallberg, R. W., & Gnanadesikan, A. (2006). The Role of Eddies in Determining the Structure and Response of the Wind-Driven Southern Hemisphere Overturning: Results from the Modeling Eddies in the Southern Ocean (MESO) Project. *Journal of Physical Oceanography*, *36*(12), 2232–2252. Retrieved from `http://journals.ametsoc.org/doi/pdf/10.1175/`

JPO2980.1http://journals.ametsoc.org/doi/abs/10.1175/JPO2980.1 doi: 10.1175/JPO2980.1

Haney, R. L. (1971). Surface thermal boundary condition for ocean circulation models. *J. phys. Oceanogr*, *1*(4), 241–248.

Hogg, A. M., Meredith, M. P., Chambers, D. P., Abrahamsen, E. P., Hughes, C. W., & Morrison, A. K. (2015, jan). Recent trends in the Southern Ocean eddy field. *Journal of Geophysical Research: Oceans*, *120*(1), 257–267. doi: 10.1002/2014JC010470

Ito, T., Woloszyn, M., & Mazloff, M. (2010). Anthropogenic carbon dioxide transport in the southern ocean driven by ekman flow. *Nature*, *463*(7277), 80–83.

Karsten, R. H., & Marshall, J. (2002). Testing theories of the vertical stratification of the Antarctic Circumpolar Current against observations. *Dynamics of Atmospheres and Oceans*, *36*(1–3), 233–246.

Kong, H., & Jansen, M. F. (2021). The impact of topography and eddy parameterization on the simulated southern ocean circulation response to changes in surface wind stress. *Journal of Physical Oceanography*, *51*(3), 825–843.

Le Quéré, C., Andrew, R. M., Friedlingstein, P., Sitch, S., Pongratz, J., Manning, A. C., ... Zhu, D. (2017). Global Carbon Budget 2017. *Earth System Science Data Discussions*, 1–79. Retrieved from https://www.earth-syst-sci-data-discuss.net/essd-2017-123/ doi: 10.5194/essd-2017-123

Marshall, J., & Radko, T. (2003). Residual-Mean Solutions for the Antarctic Circumpolar Current and Its Associated Overturning Circulation. *Journal of Physical Oceanography*, *33*(11), 2341–2354. doi: 10.1175/1520-0485(2003)033⟨2341:RSFTAC⟩2.0.CO;2

Marshall, J., & Speer, K. (2012). Closure of the meridional overturning circulation through Southern Ocean upwelling. *Nature Geoscience*, *5*(3), 171–180. Retrieved from http://oceans.mit.edu/JohnMarshall/wp-content/uploads/2013/08/Closure-of-the-meridional-overturning{_}134.pdfhttp://www.nature.com/doifinder/10.1038/ngeo1391 doi: 10.1038/ngeo1391

Mazloff, M. R., Heimbach, P., & Wunsch, C. (2010). An eddy-permitting southern ocean state estimate. *Journal of Physical Oceanography*, *40*(5), 880–899.

Meredith, M. P., Naveira Garabato, A. C., Hogg, A. M., & Farneti, R. (2012). Sensitivity of the overturning circulation in the Southern Ocean to decadal changes in wind forcing. *Journal of Climate*, *25*(1), 99–110. Retrieved from http://journals.ametsoc.org/doi/pdf/10.1175/2011JCLI4204.1 doi: 10.1175/2011JCLI4204.1

Munday, D. R., & Zhai, X. (2015). Sensitivity of Southern Ocean circulation to wind stress changes: Role of relative wind stress. *Ocean Modelling*, *95*, 15–24. Retrieved from http://dx.doi.org/10.1016/j.ocemod.2015.08.004 doi: 10.1016/j.ocemod.2015.08.004

Nikurashin, M., & Vallis, G. K. (2011). A Theory of Deep Stratification and Overturning Circulation in the Ocean. *Journal of Physical Oceanography*, *41*(3), 485–502. doi: 10.1175/2010JPO4529.1

Pedlosky, J. (1987). Geophysical Fluid Dynamics. *New York and Berlin, Springer-Verlag, 1982. 636 ...*, 742. doi: 10.1007/978-1-4612-4650-3

Rintoul, S. R. (2018). The global influence of localized dynamics in the southern ocean. *Nature*, *558*(7709), 209–218.

Sallee, J.-B., Speer, K., & Rintoul, S. (2011). Mean-flow and topographic control on surface eddy-mixing in the southern ocean. *Journal of Marine Research*, *69*(4-5), 753–777.

Stewart, A. L., & Thompson, A. F. (2013). Connecting antarctic cross-slope exchange with southern ocean overturning. *Journal of Physical Oceanography*, *43*(7), 1453–1471.

Talley, L. D. (2013). Closure of the global overturning circulation through the indian, pacific, and southern oceans: Schematics and transports. *Oceanography*,

26(1), 80–97.

Tamsitt, V., Abernathey, R. P., Mazloff, M. R., Wang, J., & Talley, L. D. (2018, mar). Transformation of Deep Water Masses Along Lagrangian Upwelling Pathways in the Southern Ocean. *Journal of Geophysical Research: Oceans*, *123*(3), 1994–2017. Retrieved from `http://doi.wiley.com/10.1002/2017JC013409` doi: 10.1002/2017JC013409

Thompson, A. F., & Naveira Garabato, A. C. (2014). Equilibration of the Antarctic Circumpolar Current by Standing Meanders. *Journal of Physical Oceanography*, *44*(7), 1811–1828. doi: 10.1175/JPO-D-13-0163.1

Viebahn, J., & Eden, C. (2012). Standing eddies in the meridional overturning circulation. *Journal of physical oceanography*, *42*(9), 1486–1508.

Viglione, G. A., & Thompson, A. F. (2016, aug). Lagrangian pathways of upwelling in the Southern Ocean. *Journal of Geophysical Research: Oceans*, *121*(8), 6295–6309. Retrieved from `http://doi.wiley.com/10.1002/2016JC011773` doi: 10.1002/2016JC011773

Young, W. R. (2012). An exact thickness-weighted average formulation of the boussinesq equations. *Journal of Physical Oceanography*, *42*(5), 692–707.

Youngs, M. K. (2020). *Residual overturning circulation and its connection to southern ocean dynamics* (Unpublished doctoral dissertation). Massachusetts Institute of Technology.

Youngs, M. K., Flierl, G. R., & Ferrari, R. (2019, nov). Role of residual overturning for the sensitivity of southern ocean isopycnal slopes to changes in wind forcing. *Journal of Physical Oceanography*, *49*(11), 2867–2881. Retrieved from `www.ametsoc.org/PUBSReuseLicenses` doi: 10.1175/JPO-D-19-0072.1

Youngs, M. K., Thompson, A. F., Lazar, A., & Richards, K. J. (2017). ACC Meanders, Energy Transfer, and Mixed Barotropic-Baroclinic Instability. *Journal of Physical Oceanography*, *47*(6), 1291–1305. doi: 10.1175/JPO-D-16-0160.1

Zhai, X., & Munday, D. R. (2014). Sensitivity of Southern Ocean overturning to wind stress changes: Role of surface restoring time scales. *Ocean Modelling*, *84*, 12–25. Retrieved from `https://ac.els-cdn.com/S1463500314001358/1-s2.0-S1463500314001358-main.pdf?{\_}tid=5dea6b1a-7a34-4552-a66b-4f38cc5fac79{\&}acdnat=1525449690{\_}f83aba3ebee77f549d718fe26c4a0547` doi: 10.1016/j.ocemod.2014.09.004